Fluid Dynamics Research

The Japan Society of Fluid Mechanics

PAPER

Oscillatory instability of 2D natural convection flow in a square enclosure with a tandem of vertically aligned cylinders

To cite this article: Yuri Feldman 2018 *Fluid Dyn. Res.* **50** 051410

IOP Publishing | The Japan Society of Fluid Mechanics Fluid *Dynamics* Research

Fluid Dyn. Res. **50** (2018) 051410 (16pp) https://doi.org/10.1088/1873-7005/aab396

Oscillatory instability of 2D natural convection flow in a square enclosure with a tandem of vertically aligned cylinders

Yuri Feldman

Department of Mechanical Engineering, Ben-Gurion University of the Negev, P.O. Box 653, Beer-Sheva 84105, Israel

E-mail: yurifeld@bgu.ac.il

Received 1 December 2017, revised 14 February 2018
Accepted for publication 2 March 2018
Published 9 August 2018

CrossMark

Communicated by: Professor Alexander Oron

Abstract

The oscillatory instability of 2D natural convection flow in a cooled square enclosure with a tandem of vertically aligned cylinders was investigated in detail. The study was performed by applying linear stability analysis and time integration of slightly perturbed flows. As a function of the distance between the two cylinders the flow underwent a transition to unsteadiness via either a symmetry-breaking or a symmetry-preserving first Hopf bifurcation. The critical values of the Rayleigh number Ra_{cr} and the oscillatory instability ω_{cr} for the transition to unsteadiness were accurately estimated. An extensive discussion of the scenarios determining the mechanisms driving the onset of the observed instabilities is presented.

Keywords: linear stability analysis, natural convection flow, tandem of vertically aligned cylinders, immersed boundary method, distributed Lagrange multiplier

(Some figures may appear in colour only in the online journal)

1. Introduction

Natural convection flow in rectangular enclosures in the presence of immersed bodies has been the subject of extensive research in the past two decades. Interest in this kind of flow was motivated by its relevance to both fundamental research and numerous engineering applications. In fact, despite relatively simple geometry, heat transfer by natural convection in rectangular enclosures exhibits a wide variety of complex dynamic behaviors, which depend on the boundary conditions (Lee *et al* 2013) and the number, position and arrangement of the immersed bodies (Park *et al* 2014, Cho *et al* 2017, Seo *et al* 2017, 2017). These behaviors may include a transition to unsteadiness via symmetry-preserving or symmetry-breaking bifurcations (Bouafia and Daube 2007, Yoon *et al* 2009) and the existence of multiple steady state regimes (Erenburg *et al* 2004). In engineering, the flow configuration under consideration is relevant to heat exchangers (Baïri *et al* 2014, Garoosi *et al* 2016), nuclear and chemical reactors (Hohnea *et al* 2006, Bieder *et al* 2015), and the cooling of electronic equipment (Peterson and Ortega 1990). Configurations with a large number of immersed bodies of different shapes and orientations are also widely used in the mesoscale analysis of natural convection flows in porous media (Martin *et al* 1998, Sangani and Yao 1998, Keyser *et al* 2006, Rochette and Clain 2006, Narvaez *et al* 2013) and comprise a computational test bed for minimizing convective heat fluxes through the boundaries of the enclosure as well as for the development of smart thermal insulating materials (Gulberg and Feldman 2016, Idan and Feldman 2017)

The investigation of natural convection within a cooled square enclosure containing a tandem of two hot circular cylinders of differing orientations, affected mainly by the mutual non-linear interactions of buoyancy flows induced by the two cylinders, is of mostly scientific interest. The steady and unsteady characteristics of this type of flow for a tandem of vertically aligned circular cylinders were elucidated by Park *et al* (2014) in terms of the spatial orientation of typical convection cells and the values of local and averaged *Nu* numbers as a function of the distance between the cylinders. The study was then extended to a tandem of two horizontally or diagonally aligned, stationary (Cho *et al* 2017) or horizontally aligned, rotating (Ashrafizadeh and Hosseinjani 2017) cylinders, with an emphasis on the characterization of unsteady scenarios in terms of the typical flow patterns and the dynamics of rising and descending plumes. The most recent results regarding the characteristics of 2D flow instability induced by natural convection in a square enclosure with four variously positioned cylinders are due to Seo *et al* (2017, 2017). In addition to describing the flow patterns typical of this kind of flow, these authors developed a heat transfer correlation determining the heat flux rate as a function of the distance between the cylinders.

Despite the very detailed investigations of the flow characteristics, including time evolution histories of the flow fields, and of the averaged *Nu* values and characterization of typical flow patterns, the previous studies have inherent drawbacks in that they focussed only on phenomenological aspects—they are all based on the findings obtained by time integration of the Navier–Stokes (NS) and energy equations. However, a full understanding of the instability mechanisms, including determination of the values of the critical Rayleigh number and the oscillating frequency, and the character of the flow bifurcation, can be reached only by performing a formal linear stability analysis. The objective of the present study was thus to address this knowledge gap by performing a formal linear stability analysis of the natural convection flow induced by a tandem of vertically aligned cylinders. The study was performed for three representative configurations, with varying distances between the cylinders. It was found that, depending on the distance between the cylinders, the natural convection flow undergoes a transition to unsteadiness via either a symmetry-breaking or a symmetry-preserving first Hopf bifurcation. The results obtained by the linear stability analysis were then extensively verified by time integration of the corresponding slightly supercritical flows. A discussion regarding the mechanisms determining the onset of each instability is presented.

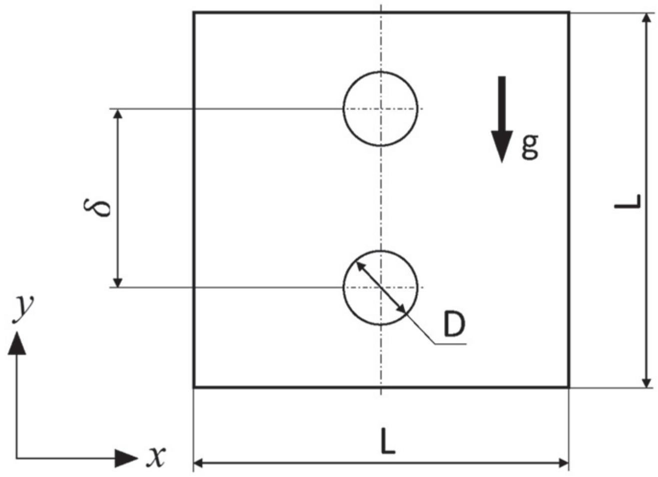

Figure 1. Schematic representation of the physical model chosen for the investigation of natural convection flow around a tandem of vertically aligned hot cylinders placed inside a cold square cavity.

2. Physical model and governing equations

The natural convection flow around a tandem of two cylinders confined in a square cavity is considered. The cylinders are aligned along the vertical centerline and are equidistant from the cavity center. The distance between the cylinder centers is equal to δ (see figure 1).

The ratio between the cylinder diameter, D, and the length of the cavity side, L, is equal to $D/L = 0.2$. Gravity acts in the negative direction to the y axis. The natural convection flow is governed by incompressible NS and energy equations (equations (1)–(3)), along with additional kinematic constraints that are summarized by equations (4)–(5); these equations are introduced to enforce the no-slip and the determined temperature (or heat flux) boundary conditions on the surfaces of the immersed cylinders:

$$\nabla \cdot \boldsymbol{u} = 0 \tag{1}$$

$$\frac{\partial \boldsymbol{u}}{\partial t} + (\boldsymbol{u} \cdot \nabla)\boldsymbol{u} = -\nabla p + \sqrt{\frac{Pr}{Ra}}\nabla^2 \boldsymbol{u} + \theta \vec{e}_y + \boldsymbol{f} \tag{2}$$

$$\frac{\partial \theta}{\partial t} + (\boldsymbol{u} \cdot \nabla)\theta = \frac{1}{\sqrt{PrRa}}\nabla^2 \theta + q \tag{3}$$

$$\boldsymbol{U}_b(\boldsymbol{X}_k) = \boldsymbol{I}(\boldsymbol{u}(\boldsymbol{x})) \tag{4}$$

$$\Theta_b(\boldsymbol{X}_k) = \boldsymbol{I}(\theta(\boldsymbol{x})), \tag{5}$$

where $\boldsymbol{u} = (u, v, w)$, p, t, and θ are the non-dimensional velocity, pressure, time and temperature, respectively, and $\vec{e}_y$ is a unit vector in the vertical (y) direction. The flow buoyancy effects are addressed by applying the Boussinesq approximation $\rho = \rho_0$ $(1\text{-}\beta(T - \mathrm{T}_c))$, which results in the appearance of an additional temperature term as a source in the momentum equation in the y direction (see equation (2)) and allows for temperature-velocity coupling. Following the works of Christon *et al* (2002) and Xin and Le Quere (2002), the problem is scaled by L, $U = \sqrt{g\beta L\Delta T}$, $t = L/U$, and $P = \rho U^2$ for length, velocity, time, and pressure, respectively, where L is the length of the square cavity, ρ is the mass density, g is the gravitational acceleration, β is the isobaric coefficient of thermal expansion, and $\Delta T = T_h - T_c$ is the temperature difference between the hot cylinder and the cold cavity surfaces. The non-dimensional temperature θ is defined as $\theta = (T - T_c)/\Delta T$. The Ra and Pr numbers are $Ra = \frac{g\beta}{\nu\alpha}\Delta TL^3$ and $Pr = \nu/\alpha$, where ν is the kinematic viscosity and α is the thermal diffusivity. All the simulations were performed for the value of $Pr = 0.7$, corresponding to air. The volumetric force $\boldsymbol{f}$ and the heat source q, appearing as sources in equations (2)–(3), reflect the impact of the immersed surfaces of the cylinders on the surrounding flow. The surfaces are determined by a series of discrete Lagrangian points, the locations of which do not necessarily coincide with the underlying Eulerian grid (for which equations (1)–(3) are formulated), and the forces and sources are additional unknowns of the overall system of equations (1)–(3). Closure of the overall system is achieved by introducing additional kinematic constraints determined by equations (4)–(5). In accordance with the formalism of the immersed boundary (IB) method, introduced by Peskin (Peskin and Flow 1972) and utilized in the present study, two adjoint operators, namely, the regularization operator $\boldsymbol{R}$ and the interpolation operator $\boldsymbol{I}$, defined as:

$$(\boldsymbol{f}, q) = R(\boldsymbol{F}^k(\boldsymbol{X}^k), Q^k(\boldsymbol{X}^k)) = \int_S (\boldsymbol{F}^k(\boldsymbol{X}^k), Q^k(\boldsymbol{X}^k)) \cdot \delta(\boldsymbol{x}_i - \boldsymbol{X}^k) dV_S^k, \tag{6a}$$

$$(\boldsymbol{U}_b, \theta_b) = I(\boldsymbol{u}(\boldsymbol{x}_i), \theta(\boldsymbol{x}_i)) = \int_\Omega (\boldsymbol{u}(\boldsymbol{x}_i), \theta(\boldsymbol{x}_i)) \cdot \delta(\boldsymbol{X}^k - \boldsymbol{x}_i) dV_{\Omega i}, \tag{6b}$$

are introduced to convey information between the Lagrangian points and the Eulerian grid. Here, S corresponds to all the Lagrangian cells that belong to the immersed body surface, Ω corresponds to a group of Eulerian cells located in the close vicinity of the immersed body surface, dV_S^k corresponds to the virtual volume encompassing each Lagrangian point k, and $dV_{\Omega i}$ is the volume of the corresponding cell of the Eulerian flow domain, whose velocity and temperature values are directly involved in enforcing the boundary conditions at point k of the immersed body. Both operators use convolutions with the Dirac delta function, δ, to facilitate the exchange of information between the Lagrangian points of the body surface and the Eulerian grid. The discrete delta function introduced by Roma *et al* (1999) was used in the present study.

$$d(r) = \begin{cases} \dfrac{1}{6\Delta r}\left[5 - 3\dfrac{|r|}{\Delta r} - \sqrt{-3\left(1 - \dfrac{|r|}{\Delta r}\right)^2 + 1}\right] & \text{for } 0.5\Delta r \leqslant |r| \leqslant 1.5\Delta r, \\ \dfrac{1}{3\Delta r}\left[1 + \sqrt{-3\left(\dfrac{|r|}{\Delta r}\right)^2 + 1}\right] & \text{for } |r| \leqslant 0.5\Delta r, \\ 0 & \text{otherwise,} \end{cases} \tag{7}$$

where Δr is the cell width in the r direction. The solution of the system of equations (1)–(5) yields the velocity, $\boldsymbol{u}$, the temperature, θ, and the pressure, p, fields along with the field of Lagrangian volumetric forces, $\boldsymbol{F}_k$, and heat fluxes, Q_k, determined for each volume, dV_S^k. The linear stability eigenproblem is formulated by assuming infinitesimally small perturbations of the form $\{\tilde{\boldsymbol{u}}(x, y), \tilde{\theta}(x, y), \tilde{p}(x, y), \tilde{\boldsymbol{F}}(x, y), \tilde{Q}(x, y)\}e^{\lambda t}$ around the steady state flow $\boldsymbol{U}, \Theta, \boldsymbol{P}, \boldsymbol{F}, Q$, as follows:

$$\lambda\tilde{\boldsymbol{u}} = -(\boldsymbol{U} \cdot \nabla)\tilde{\boldsymbol{u}} - (\tilde{\boldsymbol{u}} \cdot \nabla)\boldsymbol{U} - \nabla\tilde{p} + \sqrt{\frac{Pr}{Ra}}\nabla^2\tilde{\boldsymbol{u}} - \tilde{\theta}\overrightarrow{e_y} + R_{\tilde{\boldsymbol{F}}}, \tag{8a}$$

$$\lambda\tilde{\theta} = -(\boldsymbol{U}\cdot\nabla)\tilde{\theta} - (\tilde{\boldsymbol{u}}\cdot\nabla)\Theta + \frac{1}{\sqrt{PrRa}}\nabla^2\tilde{\theta} + R_{\tilde{Q}}, \tag{8b}$$

$$0 = \nabla\cdot\tilde{\boldsymbol{u}}, \tag{8c}$$

$$0 = I(\tilde{\boldsymbol{u}}), \tag{8d}$$

$$0 = I(\tilde{\theta}). \tag{8e}$$

The generalized eigenproblem formulated in equations (8(a)–(e)) with all homogeneous boundary conditions is then solved by applying the shift-and-invert Arnoldi iteration:

$$(\boldsymbol{J} - \sigma\boldsymbol{B})^{-1}\boldsymbol{B}\begin{bmatrix}\tilde{\boldsymbol{u}}\\ \tilde{\theta}\\ \tilde{p}\\ \tilde{\boldsymbol{F}}\\ \tilde{Q}\end{bmatrix} = \mu\begin{bmatrix}\tilde{\boldsymbol{u}}\\ \tilde{\theta}\\ \tilde{p}\\ \tilde{\boldsymbol{F}}\\ \tilde{Q}\end{bmatrix}, \qquad \mu = \frac{1}{\lambda - \sigma}, \tag{9}$$

where $\boldsymbol{J}$ is the Jacobian matrix calculated from the RHS of equations (8(a)–(e)), and $\boldsymbol{B}$ is the diagonal matrix whose diagonal elements, corresponding to the values of $\tilde{\boldsymbol{u}}$ and $\tilde{\theta}$, are equal to unity, and whose diagonal elements, corresponding to $\tilde{p}$, $\tilde{\boldsymbol{F}}$ and $\tilde{Q}$, are equal to zero (see Gelfgat 2007, Feldman and Gulberg 2016 for more details). The solution of the generalized eigenproblem yields the critical Rayleigh value, Ra_{cr} at which the real part of the complex leading eigenvalue λ is equal to zero (to a prescribed precision), i.e. $Real(\lambda) = 0$. When shift-and-invert Arnoldi iteration is applied, the leading eigenvalue λ is inversely related to the dominant eigenvalue μ corrected by the value of a complex shift σ (see equation (9)). The critical values are obtained by utilizing the secant method. Next, we define the Nusselt number Nu as a ratio of convective to conductive fluxes. Utilizing the same scaling as in equations (1)–(5), the non-dimensional heat flux from the finite surface of the immersed body with an area encircling any Lagrangian point k is defined as:

$$\left(\frac{\partial\theta}{\partial\hat{n}}\right)_k = \Delta x\sqrt{PrRa}\,Q_k, \tag{10}$$

where Q_k is the k^{th} Lagrangian volumetric heat flux obtained as a part of a solution of the system of equations (1)–(5). The heat flux values averaged over the entire surface of the immersed body are then used for the calculation of the average Nusselt number, $\overline{Nu}$, defined as:

$$\overline{Nu} = \overline{\frac{\partial\theta}{\partial\hat{n}}}. \tag{11}$$

3. Implementation details

The governing equations (1)–(5) are discretized by a standard finite volume method (Patankar 1980) on a staggered grid. Diffusion, pressure, and terms corresponding to the force and the heat flux densities are treated implicitly, while all the non-linear advection terms are treated explicitly and taken from the previous time step. The time derivative in the momentum and the energy equations is approximated by a second-order backward finite difference. The above spatial and temporal discretizations result in a full coupling between all the flow fields

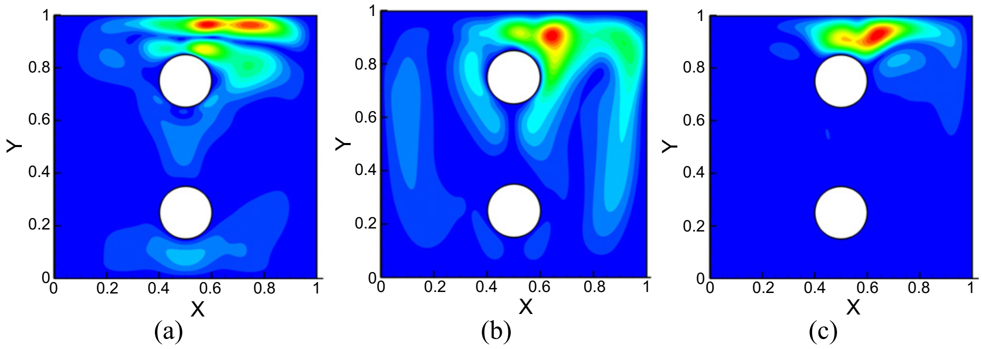

Figure 2. Contours of the absolute values of the leading eigenmode obtained at $Ra_{cr} = 5.011 \times 10^5$ and $\delta = 0.5$ on a 1800×1800 grid for: (a) x-velocity component, $|u'|$; (b) y-velocity component, $|v'|$; temperature, $|\theta'|$. Reprinted from Feldman and Gulberg (2016), Copyright (2016), with permission from Elsevier.

(including additionally introduced force and heat flux densities). The fully coupled approach automatically yields a divergence free velocity field for both time integration and Arnoldi iteration. Comprising a straight-forward extension of the fully pressure-velocity coupled approach introduced in Feldman and Gelfgat (2009) and the linear stability procedure developed in Gelfgat (2007), the present study also utilizes the direct MUMPS solver (Amestoy *et al* 2001, 2006) for performing time integration and the shift-and-invert Arnoldi iteration, both extended by the IB capability. For further details of the extensive verification of the utilized approach for the analysis of natural convection confined flows in the presence of immersed bodies, our previous study (Feldman and Gulberg 2016) should be consulted.

4. Results and discussion

We start with an analysis of configuration characterized by the value of $\delta = 0.5$ (see figure 1). The linear stability analysis for this configuration has already been performed in our previous study (Feldman and Gulberg 2016) and is summarized in brief here for the sake of completeness. According to the performed linear stability analysis, the flow under consideration undergoes a transition to unsteadiness via the first Hopf bifurcation. Figure 2 presents the contours of the absolute values of the temperature and the velocity leading eigenmodes[1] obtained at the critical Rayleigh, $Ra_{cr} = 5.011 \times 10^5$, and critical angular frequency, $\omega_{cr} = 0.2875$, values. The grid convergence study with respect to the obtained Ra_{cr} and ω_{cr} values is summarized in table 1.

The distributions of all the perturbations are biased to the right, clearly indicating the symmetry-breaking character of the bifurcation. To confirm the findings obtained by the linear stability analysis, we performed a time integration of the natural convection flow in the slightly supercritical regime at $Ra = 1.1 \times Ra_{cr} = 5.51 \times 10^5$. The temperature, pressure and velocity fields of the unstable steady state obtained at $Ra_{cr} = 5.011 \times 10^5$ were taken as the initial condition. All the time integration results presented in this paper were obtained on 400×400 grids. By ensuring that further grid refining leads to insignificant deviations (less

[1] Spatial distribution of the obtained eigenmodes can, in general, be multiplied by any positive constant, as it corresponds to the intensity of oscillations which will be observed when performing time integration of slightly bifurcated flow.

Table 1. Grid convergence for the critical Ra_{cr} and ω_{cr} values, $\delta = 0.5$.

Grid	$Ra_{cr} \times 10^5$	ω_{cr}
1400 × 1400	5.015	0.2873
1600 × 1600	5.012	0.2874
1800 × 1800	5.011	0.2875
2000 × 2000	5.011	0.2875

than 0.5% for the averaged $\overline{Nu}$ values and less than 1% for all the flow fields), we successfully verified the grid independence of the results (see tables 2 and 3 for the detailed comparison).

The time evolution and the amplitude spectrum of the Nusselt values $\overline{Nu}$ averaged over the surfaces of the upper and lower cylinders are presented in figure 3. It is clear that the $\overline{Nu}$ values of both cylinders oscillate with the same oscillating frequency, corresponding to the main harmonic characterized by the angular frequency value equal to $\omega = 0.258$, which is close to the value of $\omega_{cr} = 0.2875$ predicted by the linear stability analysis. Note also the existence of the main harmonic multipliers clearly seen in the amplitude spectrum of both Nusselt values, which is a consequence of the non-linearity of the flow in the supercritical regime. It should be noted that the flow non-linearity is more pronounced in the vicinity of the lower cylinder, which is characterized by relatively low values of the perturbations. The mechanism driving the observed instability can be revealed by examining the instantaneous characteristics of the slightly bifurcated flow. Figure 4 presents a series of pathline snapshots taken at four representative points (1, 2, 3, 4) evenly distributed over a single period of $\overline{Nu}$ of the upper cylinder (see figure 3(a)). It is clear that the instability results from the interaction of the two counter rotating vortices that are formed immediately above the upper cylinder. The dimensions of the two vortices vary over the period: the growth of the left vortex is accompanied by shrinkage and consequent shedding of the right one, which explains the origin of the symmetry-breaking bifurcation predicted by the linear stability analysis.

The next step of the study focussed on a qualitative and quantitative investigation of the effect of the distance between the cylinders on the properties of the observed bifurcation. To investigate this effect, we performed the same numerical simulations (i.e. linear stability analysis followed by time integration of slightly bifurcated flow) for two additional configurations with δ values smaller and larger than $\delta = 0.5$, namely, for $\delta = 0.4$ and $\delta = 0.6$.

We first discuss the results obtained for the configuration with $\delta = 0.4$. The contours of the absolute values of the obtained temperature and the velocity leading eigenmodes are shown in figure 5. For this configuration, the converged critical Rayleigh and angular frequency values (see table 4) are equal to $Ra_{cr} = 2.562 \times 10^5$ and $\omega_{cr} = 0.2397$. Reducing the value of δ from $\delta = 0.5$ to $\delta = 0.4$ does not qualitatively affect the patterns of the temperature and the velocity leading eigenmodes, thereby preserving the symmetry-breaking character of the bifurcation. This observation is also confirmed by the qualitative similarity between the time evolutions and the amplitude spectra of the averaged $\overline{Nu}$ values presented in figure 6 for $\delta = 0.4$ and their corresponding counterparts obtained for $\delta = 0.5$, as shown in figure 3.

Nonetheless, a decrease in the δ value results in about a twofold decrease in the value of the critical Rayleigh number, Ra_{cr} and in about a 20% decrease in the value of the critical angular frequency, $\omega_{cr} = 0.2397$. Dependance of the Ra_{cr} value on the distance between the two cylinders is governed by two competing mechanisms. First, the closer the cylinders are, the smaller the distance is that accelerating thermal plume rising from the lower cylinder can pass without being suppressed by the surface of the upper cylinder. Second, as the distance between the two cylinders decreases, their remoteness from the bottom and top horizontal

Table 2. Comparison between the maximal and the minimal values of the averaged $\overline{Nu}$ values obtained on 400×400 and 500×500 grids for the upper and lower cylinders.

$\delta = 0.4$, $Ra = 2.761 \times 10^5$							
$\overline{Nu}_{\max_{up}}$		$\overline{Nu}_{\min_{up}}$		$\overline{Nu}_{\max_{low}}$		$\overline{Nu}_{\min_{low}}$	
400×400	500×500	400×400	500×500	400×400	500×500	400×400	500×500
8.4437	8.4466	7.2063	7.1901	14.506	14.483	14.351	14.324
$\delta = 0.5$, $Ra = 5.51 \times 10^5$							
$\overline{Nu}_{\max_{up}}$		$\overline{Nu}_{\min_{up}}$		$\overline{Nu}_{\max_{low}}$		$\overline{Nu}_{\min_{low}}$	
400×400	500×500	400×400	500×500	400×400	500×500	400×400	500×500
11.199	11.194	9.768	9.748	17.072	17.043	16.963	16.930
$\delta = 0.6$, $Ra = 1.41 \times 10^6$							
$\overline{Nu}_{\max_{up}}$		$\overline{Nu}_{\min_{up}}$		$\overline{Nu}_{\max_{low}}$		$\overline{Nu}_{\min_{low}}$	
400×400	500×500	400×400	500×500	400×400	500×500	400×400	500×500
14.173	14.163	13.969	13.956	20.867	20.825	20.843	20.801

Table 3. Comparison between the maximal and the minimal values of the flow characteristics obtained on 400 × 400 and 500 × 500 grids.

	$\delta = 0.4$, $Ra = 2.761 \times 10^5$				$\delta = 0.5$, $Ra = 5.51 \times 10^5$				$\delta = 0.6$, $Ra = 1.41 \times 10^6$			
	CP (0.25, 0.25)		CP (0.75, 0.75)		CP (0.25, 0.25)		CP (0.75, 0.75)		CP (0.25, 0.25)		CP (0.75, 0.75)	
	Grid		Grid		Grid		Grid		Grid		Grid	
	400 × 400	500 × 500	400 × 400	500 × 500	400 × 400	500 × 500	400 × 400	500 × 500	400 × 400	500 × 500	400 × 400	500 × 500
max(u_x)	0.08567	0.08534	0.1265	0.1271	0.06461	0.06432	−0.05346	−0.05384	0.01636	0.01623	−0.01301	−0.01301
min(u_x)	0.08291	0.08228	0.07312	0.07252	0.0528	0.05269	−0.06404	−0.06409	0.01301	0.01301	−0.01636	−0.01623
max(u_y)	0.05182	0.051565	0.1144	0.1133	0.07187	0.072	0.07179	0.0718	0.05067	0.05045	0.05067	0.05044
min(u_y)	0.04454	0.04469	0.07821	0.07783	0.06446	0.06423	0.06385	0.06364	0.045	0.045	0.045	0.04501
max(θ)	0.2223	0.2233	0.5982	0.6051	0.2456	0.2471	0.501	0.5011	0.2252	0.2252	0.2252	0.2252
min(θ)	0.2137	0.2129	0.5323	0.5334	0.2332	0.2331	0.2387	0.2402	0.2174	0.2175	0.4335	0.4334

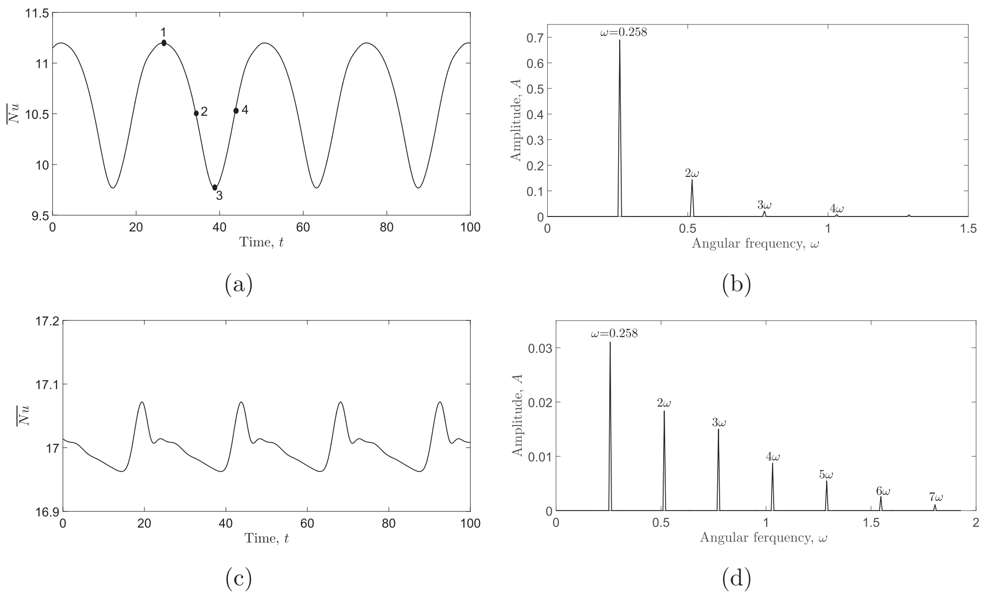

Figure 3. Time evolution results obtained for $\delta = 0.5$, at $Ra = 5.51 \times 10^5$: (a) $\overline{Nu}$ value averaged over the surface of the upper cylinder; (b) amplitude spectrum obtained for $\overline{Nu}$ averaged over the surface of the upper cylinder; (c) $\overline{Nu}$ value averaged over the surface of the lower cylinder; (d) amplitude spectrum obtained for $\overline{Nu}$ averaged over the surface of the lower cylinder.

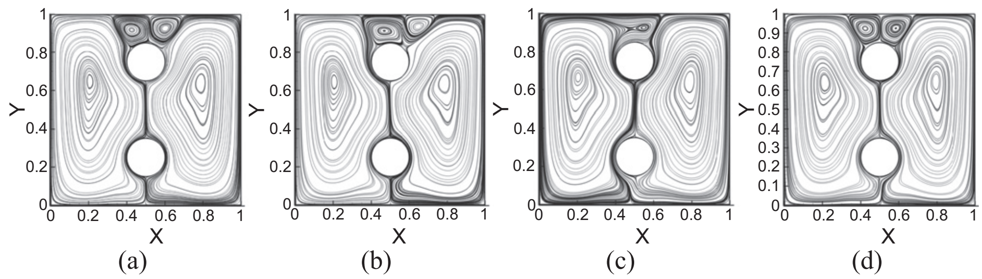

Figure 4. Characteristics of the periodic natural convection flow developing around the tandem of vertically aligned cylinders characterized by the value of $\delta = 0.5$ at $Ra = 5.51 \times 10^5$: (a)–(d) instantaneous pathlines at the selected time instances [1, 2, 3, 4].

boundaries of the cavity increases. As a result, a thermal plume rising from the upper cylinder has more space to accelerate before it reaches the top surface of the cavity. In addition, the increasing distance between the lower cylinder and the bottom surface of the cavity enables a higher momentum to be preserved while the flow changes its direction in this region. A significant decrease in the Ra_{cr} value, when decreasing the distance between the cylinders, can be explained by a dominance of the second mechanism.

Note also that while the amplitude of the main harmonic of the upper cylinder $\overline{Nu}$ obtained for $\delta = 0.4$ is about 20% lower than the corresponding $\overline{Nu}$ value obtained for $\delta = 0.5$, the opposite trend is observed for the $\overline{Nu}$ amplitude obtained for the lower cylinder,

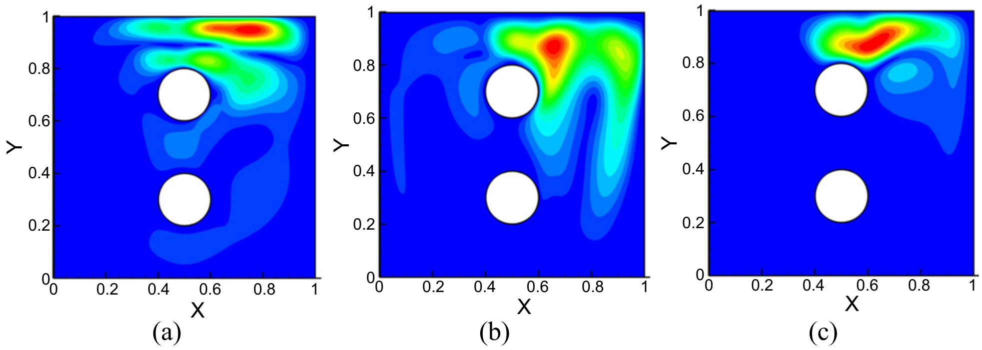

Figure 5. Contours of the absolute values of the leading eigenmode obtained at $Ra_{cr} = 2.562 \times 10^5$ and $\delta = 0.4$ on a 1800×1800 grid for: (a) x-velocity component, $|u'|$; (b) y-velocity component, $|v'|$; temperature, $|\theta'|$.

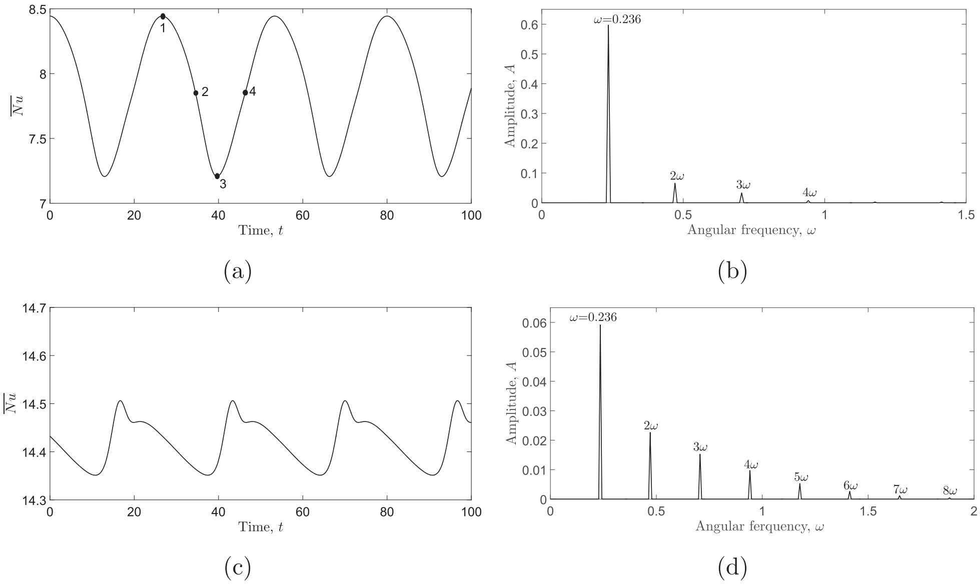

Figure 6. Time evolution results obtained for $\delta = 0.4$, at $Ra = 2.761 \times 10^5$: (a) $\overline{Nu}$ value averaged over the surface of the upper cylinder; (b) amplitude spectrum obtained for $\overline{Nu}$ averaged over the surface of the upper cylinder; (c) $\overline{Nu}$ value averaged over the surface of the lower cylinder; (d) amplitude spectrum obtained for $\overline{Nu}$ averaged over the surface of the lower cylinder.

Table 4. Grid convergence for the critical Ra_{cr} and ω_{cr} values, $\delta = 0.4$.

Grid	$Ra_{cr} \times 10^5$	ω_{cr}
1400×1400	2.564	0.2398
1600×1600	2.561	0.2295
1800×1800	2.562	0.2397
2000×2000	2.562	0.2397

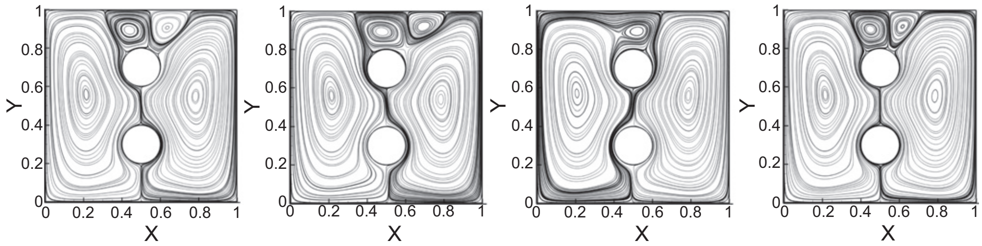

Figure 7. Characteristics of the periodic natural convection flow developing around the tandem of vertically aligned cylinders characterized by the value of $\delta = 0.4$ at $Ra = 2.761 \times 10^5$: (a)–(d) instantaneous pathlines at the selected time instances [1, 2, 3, 4].

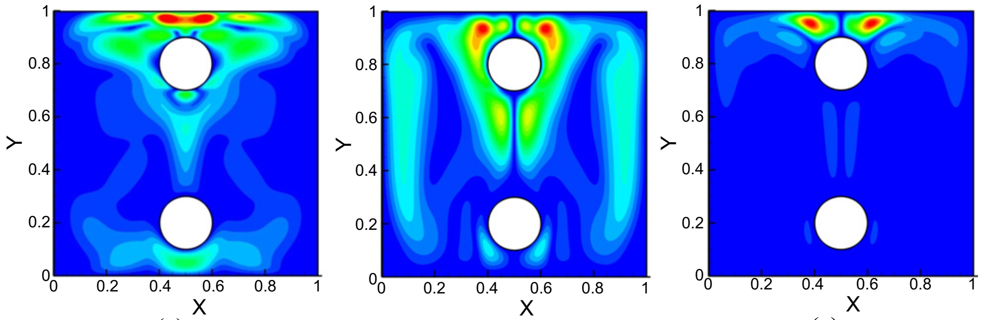

Figure 8. Contours of the absolute values of the leading eigenmode obtained at $Ra_{cr} = 1.285 \times 10^6$ and $\delta = 0.6$ on a 1800×1800 grid for: (a) x-velocity component, $|u'|$; (b) y-velocity component, $|v'|$; temperature, $|\theta'|$.

namely, the amplitude of the main harmonic of the lower cylinder $\overline{Nu}$ obtained for $\delta = 0.4$ is about twice that obtained for the value of $\delta = 0.5$. This observation can be explained by examining the instantaneous pathlines of the slightly bifurcated natural convection flow, as shown in figure 7. Similarly to the configuration characterized by the value of $\delta = 0.5$, it can be seen that instability observed for the present configuration is also driven by the interaction of the pair of counter rotating vortices. However, in this configuration the vortices are larger than those observed for $\delta = 0.5$, which apparently leads to longer time-over times and results in lower frequency and amplitude values of the main $\overline{Nu}$ harmonic.

Let us examine the configuration characterized by $\delta = 0.6$. The contours of the absolute values of the temperature and the velocity leading eigenmodes (see figure 8) lead us to the conclusion that the instability of this flow is driven by a mechanism that differs from that for the two previous configurations. In fact, the flow undergoes a transition to unsteadiness at a significantly (an order of magnitude) higher Ra_{cr} value (see table 5) and, importantly, the temperature and the velocity perturbations of the flow are globally reflectional and symmetrical with respect to the cavity vertical centerline. In addition, there are two distinctive features of the flow under consideration that should be pointed out. The first is that the oscillating frequency of the $\overline{Nu}$ values obtained for the upper and lower cylinders is twice that predicted by the linear stability analysis (see figure 9). The second is related to the dynamics

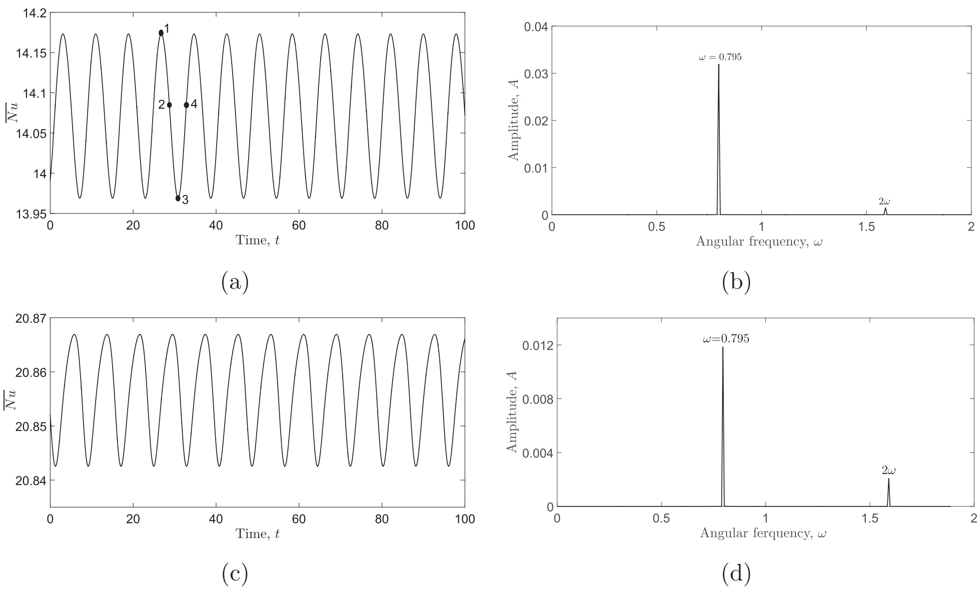

Figure 9. Time evolution results obtained for $\delta = 0.6$, at $Ra = 1.41 \times 10^6$: (a) $\overline{Nu}$ value averaged over the surface of the upper cylinder; (b) amplitude spectrum obtained for $\overline{Nu}$ averaged over the surface of the upper cylinder; (c) $\overline{Nu}$ value averaged over the surface of the lower cylinder; (d) amplitude spectrum obtained for $\overline{Nu}$ averaged over the surface of the lower cylinder.

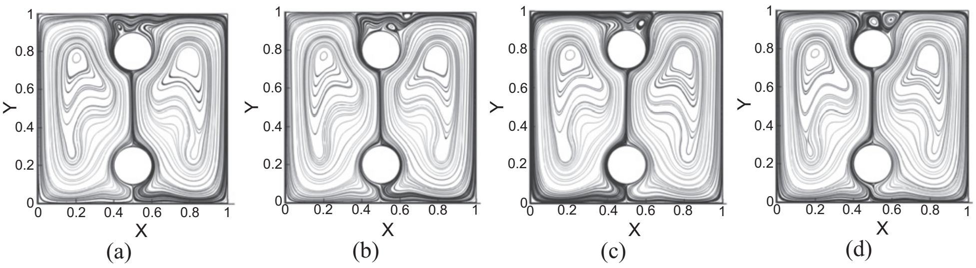

Figure 10. Characteristics of the periodic natural convection flow developing around the tandem of vertically aligned cylinders characterized by the value of $\delta = 0.6$ at $Ra = 1.41 \times 10^6$: (a)–(d) instantaneous pathlines at the selected time instances [1, 2, 3, 4].

Table 5. Grid convergence for the critical Ra_{cr} and ω_{cr} values, $\delta = 0.6$.

Grid	$Ra_{cr} \times 10^6$	ω_{cr}
1400 × 1400	1.282	0.3740
1600 × 1600	1.284	0.3718
1800 × 1800	1.285	0.3701
2000 × 2000	1.285	0.3691

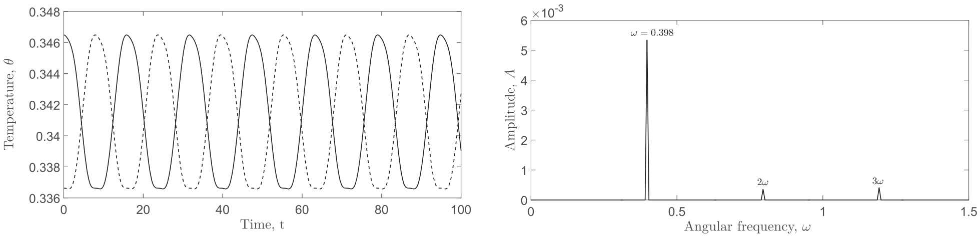

(a) (b)

Figure 11. Monitoring the history of temperature, $\delta = 0.6$, $Ra = 1.41 \times 10^6$: (a) time evolution of temperature, θ, monitored at control point (0.5, 0.425)—full line and control point (0.5 0.575)—dashed line; (b) amplitude spectrum of the temperature history monitored at the two control points.

of the slightly bifurcated flow presented in figure 10; the qualitative difference between the dynamics of the flow and that of the two previous configurations can be pinpointed by following the dynamics of the thermal plume rising from the upper cylinder. It can be seen that over a single oscillating period the thermal plume twists twice in diametrically opposite directions, directing the heat fluxes along the cavity's top wall to the left and then to the right top corners of the cavity. All the above qualitative observations suggest that the observed flow is invariant under the action of spatiotemporal symmetry H (half a period apart) preserving the Z_2 symmetry group (Kuznetsov 1998) and formally reading

$$\boldsymbol{H}\boldsymbol{u}(\boldsymbol{X}', t) = K_{\boldsymbol{Z}'}(\boldsymbol{X}, t + T/2) = (u_{X'}, u_{Y'}, -u_{Z'})(X', Y', -Z', t + T/2), \tag{12}$$

with the H-symmetric base flow $\boldsymbol{H}\bar{\boldsymbol{u}}(\boldsymbol{X}') = K_{Z'}\bar{\boldsymbol{u}}'(\boldsymbol{X}')$, where $K_{Z'}$ is the spatial reflection: $Z' \to -Z'$, $u_{Z'} \to -u_{Z'}$ and T is period of the perturbed flow oscillations dynamically determined by the corresponding Ra number. In isothermal 2D flows, a representative example of this symmetry is the von Karman street wake, whose symmetries are discussed in detail in Barkley *et al* (2000) and Blackburn *et al* (2005). To quantitatively prove that the natural convection flow under consideration also preserves the Z_2 symmetry group (half a period apart), we monitored the history of the temperature values at two points positioned symmetrically from the two sides of the cavity centerline, as shown in figure 11. It can clearly be recognized that, first, the oscillating frequency of both signals is now close to that predicted by the linear stability analysis and, second, the signals are precisely half a period apart, thereby identifying the present flow with the Z_2 symmetry group. It can therefore be concluded that similarly to the flow around the cylinder, the observed instability is also driven by a vortex shedding mechanism.

5. Concluding remarks

The mechanism of oscillatory instability of 2D natural convection flow in a cooled square enclosure, with a tandem of hot vertically aligned cylinders, was studied by both linear stability analysis and time integration of the supercritical flow. The critical values of the Rayleigh number, Ra_{cr} and the angular oscillating frequency, ω_{cr}, were accurately estimated. The dependance of the Ra_{cr} and ω_{cr} values on the distance between the cylinders was investigated and explained both qualitatively and quantitatively.

It was found that the configuration under consideration exhibits a transition to unsteadiness via the first Hopf bifurcation, which can be either symmetry-breaking or symmetry-preserving. The specific scenario depends on the distance between the cylinders. The symmetry-breaking bifurcation is driven by the interaction between a pair of counter rotating vortices that are formed immediately above the upper cylinder. The symmetry-preserving bifurcation belongs to the Z_2 symmetry group and similarly, the flow around the cylinder is driven by a vortex shedding mechanism. This study thus constitutes a significant milestone toward further extending the performed analysis to fully 3D configurations with all no-slip boundaries, which will be the focus of our future research.

References

Amestoy P R, Duff I S, Koster J and L'Excellent J-Y 2001 A fully asynchronous multifrontal solver using distributed dynamic scheduling *SIAM Journal of Matrix Analysis and Applications* **23** 15–41

Amestoy P R, Guermouche A, L'Excellent J-Y and S Pralet S 2006 Hybrid scheduling for the parallel solution of linear systems *Parallel Comput.* **32** 136–56

Ashrafizadeh A and Hosseinjani A A 2017 A phenomenological study on the convection heat transfer around two enclosed rotating cylinders via an immersed boundary method *Int. J. Heat Mass Transf.* **107** 667–85

Baïri A, Zarco-Pernia E and García De Mara J M 2014 A review on natural convection in enclosures for engineering applications. The particular case of the parallelogrammic diode cavity *Appl. Therm. Eng.* **63** 304–22

Barkley D, Tuckerman L S and Golubitsky M 2000 Bifurcation theory for three-dimensional flow wake of a circular cylinder *Phys. Rev.* E **61** 5247–52

Bieder U, Falk F and Fauchet G 2015 CFD analysis of the flow in the near wake of a generic PWR mixing grid *Abbals Nucl. Energy.* **82** 169–78

Blackburn H M, Marques F and Lopez J 2005 Symmetry breaking of two-dimensional time-periodic wakes *J. Fluid Mech.* **522** 395–411

Bouafia M and Daube O 2007 Natural convection for large temperature gradients around a square solid body within a rectangular cavity *Int. J. Heat Mass Transf.* **50** 3599–615

Cho H W, Seo Y M, Gi S M, Man Y H and Park Y G 2017 The effect of instability flow for two-dimensional natural convection in a square enclosure with different arrays of two inner cylinders *Int. J. Heat Mass Transf.* **114** 307–17

Christon M, Gresho P and Sutton S 2002 Computational predictability of time-dependent natural convection flows in enclosures (including a benchmark solution) *Int. J. Numer. Meth. Fluids* **40** 953–80

Erenburg V, Gelfgat A Yu, Kit E, Bar-Yoseph P Z and Solan A 2004 Multiple states, stability and bifurcations of natural convection in rectangular cavity with partially heated vertical walls *J. Fluid Mech.* **492** 63–89

Feldman Yu and Gelfgat A Yu 2009 On pressure-velocity coupled time-integration of incompressible Navier–Stokes equations using direct inversion of Stokes operator or accelerated multigrid technique *Comput. Struct.* **87** 710–20

Feldman Y and Gulberg Y 2016 An extension of the immersed boundary method based on the distributed Lagrange multiplier approach *J. Comput. Phys.* **322** 248–66

Garoosi F, Hoseininejad F and Rashidi M M 2016 Numerical study of natural convection heat transfer in a heat exchanger filled with nanofluids *Energy* **109** 664–78

Gelfgat A Y 2007 Stability of convective flows in cavities: solution of benchmark problems by a low-order finite volume method *Int. J. Numer. Meth. Fluids* **53** 485–506

Gulberg Y and Feldman Yu 2016 Flow control through use of heterogeneous porous media: smart passive thermo-insulating materials *Int. J. Therm. Scien.* **110** 369–82

Hohnea T, Kliema S and Bieder U 2006 Modeling of a buoyancy-driven flow experiment at the ROCOM test facility using the CFD codes CFX-5 and Trio−U *Nucl. Engin. Design.* **236** 1309–25

Idan S and Feldman Yu 2017 Smart passive thermal insulation of confined natural convection heat transfer: an application to hollow construction blocks *Appl. Therm. Eng.* **124** 1328–42

Keyser M J, Conradie M, Coertzen M and Van Dyk J C 2006 Effect of coal particle size distribution on packed bed pressure drop and gas flow distributions *Fuel* **85** 1439–45

Kuznetsov Y A 1998 *Elements of Applied Bifurcation Theory* 2nd edn (New York: Springer) 273–88

Lee H J, Doo J H, Ha M Y and Yoon H S 2013 Effects of thermal boundary conditions on natural convetion in asquare enclosure with an inner circular locally heated from the bottom wall *Int. J. Heat Mass Transf.* **65** 3460–9

Martin A R, Saltiel C and Shyy W 1998 Frictional losses and convective heat transfer in sparse, periodic cylinder arrays in cross flow *Int. J. Heat Mass Transf.* **41** 2382–97

Narvaez A, Yazdchi K, Luding S and Harting J 2013 From creeping to inertial flow in porous media: a lattice boltzmann finite element study *J. Stat. Mech: Theory Exp.* **2013** P02038

Park Y, Ha M, Choi C and Park J 2014 Natural convection in a square enclosure with two inner circular cylinders positioned at different vertical locations *Int. J. Heat Mass Transf.* **77** 501–18

Patankar S V 1980 *Numerical Heat Transfer and Fluid Flow* (New York: McGraw-Hill)

Peskin C and Flow S 1972 patterns around heart valves: a numerical method *J. Comput. Phys.* **10** 252–71

Peterson G P and Ortega A 1990 Thermal control of electronic equipment and devices *Adv. Heat Transf.* **20** 181–314

Rochette D and Clain S 2006 Two-dimensional computation of gas flow in porous bed characterized by a porosity jump *J. Comput. Phys.* **219** 104–19

Roma A, Peskin C S and Berger M J 1999 An adaptive version of the immersed boundary method *J. Comput. Phys.* **153** 509–34

Sangani A S and Yao C 1998 Transport process in random arrays of cylinders. II *Viscous flow. Phys. Fluid.* **31** 2435–44

Seo Y M, Park Y G, Kim M, Hyun S Y and Man Y H 2017 Two-dimensional flow instability induced by natural convection in a square enclosure with four inner cylinders: I. Effect of horizontal position of inner cylinders *Int. J. Heat Mass Transf.* **113** 1306–18

Seo Y M, Mun G S, Park Y G and Man Y H 2017 Two-dimensional flow instability induced by natural convection in a square enclosure with four inner cylinders: II. Effect of various positions of inner cylinders *Int. J. Heat Mass Transf.* **113** 1319–31

Xin S and Le Quere P 2002 An extended Chebyshev pseudo-spectral benchmark for the 8:1 differentially heated cavity *Int. J. Numer. Meth. Fluids* **40** 981–98

Yoon H S, Ha M Y, Byung S K and Yu D H 2009 Effect of the position of a circular cylinder in a square enclosure on natural convection at Rayleigh number of 10^7 *Phys. Fluid.* **21** 047101